Gene-in-gene coding generates a dual-isoform condensate that promotes the ecological resilience of *Vibrio cholerae*

Running title: Dual coding drives *Vibrio* success

Tong-Tong Pei[1], Qiao-Yu Chen[1], Xing-Yu Wang[1, 2], Amy Ma[3#], Jia-Xin Liang[1], Zi-Yan Ye[1], Yu-Zhao Liu[1], Jing-Tong Su[1], Xiaoye Liang[1], Ying An[1], Jun Zhu[3], Tao Dong[1]*

Affiliations:

[1] Department of Immunology and Microbiology, School of Life Sciences, Guangming Advanced Research Institute, Southern University of Science and Technology, Shenzhen, Guangdong, 518055, China

[2] State Key Laboratory of Microbial Metabolism, Joint International Research Laboratory of Metabolic & Developmental Sciences, School of Life Sciences and Biotechnology, Shanghai Jiao Tong University, Shanghai, 200240, China

[3] Department of Microbiology, Perelman School of Medicine, University of Pennsylvania, Philadelphia, Pennsylvania, 19104, USA

* Corresponding Email: dongt@sustech.edu.cn

Current address: Department of Microbiology and Immunology, Drexel University College of Medicine, Philadelphia, Pennsylvania, 19104, USA

Keywords: protein secretion, Fha, T6SS, *Vibrio cholerae*, phase separation

Abstract

While eukaryotes employ alternative splicing to diversify protein functions, analogous strategies in bacteria remain underexplored. Here we identify a conserved intragenic coding mechanism in *Vibrio cholerae* that generates two isoforms of the essential scaffold Fha and show that these isoforms cooperate through liquid–liquid phase separation to regulate the type VI secretion system (T6SS). The full-length isoform, Fha^{L}, seeds assembly by engaging the membrane complex, whereas an internally translated isoform, Fha^{S}, enhances secretion efficiency by strengthening specific interactions with baseplate components. This isoform partitioning is ecologically critical; a mutant producing only Fha^{L} is impaired in bacterial competition, susceptible to eukaryotic predation, and defective in host colonization. Both isoforms form condensates, and a single residue change within a C-terminal helix abolishes condensate formation and significantly reduces T6SS activities. The internal translation and condensate-forming residues are strictly conserved across >10,000 *V. cholerae* isolates and active in diverse *Vibrio* species. These findings define a translational–biophysical mechanism that tunes a widespread contractile protein nanomachine for ecological success.

Introduction

One of biology's most striking themes for expanding functional complexity is to extract new functions from existing genetic material rather than simply increasing genome size. In eukaryotes, alternative splicing generates protein isoforms from single genes, while liquid–liquid phase separation (LLPS) enables proteins and RNAs to self-organize into dynamic condensates that spatially and temporally coordinate key cellular processes [1-3]. In bacteria, internal translation and overlapping coding sequences can likewise generate multiple protein products from single loci, but their molecular mechanisms are poorly defined and seldom explored in the context of biophysical processes like LLPS [4-7]. Whether bacteria have evolved strategies that simultaneously exploit compact coding architectures and condensate-based regulation remains unknown.

As the causative agent of cholera, *Vibrio cholerae* has fueled seven pandemics and continues to threaten global health, while thriving in aquatic natural reservoirs [8-10]. Its success depends on a suite of virulence and adaptation mechanisms, among which the type VI secretion system (T6SS) is central [11,12]. This contractile nanomachine assembles into a cell-spanning and membrane-anchored spear-like structure and injects toxic effectors into competitors and host cells, providing both ecological advantage and pathogenic potential [13,14]. Despite its importance, the molecular events that initiate and regulate T6SS assembly remain poorly understood [15,16]. In *Acidovorax citrulli*, the scaffold protein Fha and its cognate kinase PpkA undergo LLPS and coordinate the initiation of an "inside-out" mode of T6SS assembly [17,18]. However, a direct causal link between LLPS and assembly has yet to be established. Moreover, *V. cholerae* lacks a homologous kinase, raising the question of how Fha functions in systems that lack upstream regulatory enzymes and whether condensates play a mechanistic role.

However, dissecting the causal role of LLPS in bacterial systems remains challenging. Even point mutations that disrupt condensates inevitably alter the native protein sequence and may introduce secondary effects on folding, stability, or partner recognition. Recent advances in *de novo* protein design offer a powerful approach to overcome these limitations. AI-driven platforms such as RFdiffusion and ProteinMPNN can generate protein binders that engage specific structural motifs for modulating LLPS behaviors [19-22]. These tools provide an orthogonal way to perturb bacterial condensates and their associated assembly of complex protein machineries.

Here we show that *V. cholerae* employs in-frame tandem translation within *fha* to produce two isoforms, a full-length Fha^{L} and a shorter Fha^{S}. These isoforms partition function, with Fha^{L} required for initiation of T6SS assembly and Fha^{S} enhancing efficiency, microbial competition, and host colonization. Both isoforms undergo LLPS, and a single amino acid substitution (L341A) within a C-terminal helix abolishes condensate formation and sharply reduces T6SS activity. We designed *de novo* protein binders using RFdiffusion–ProteinMPNN to selectively target this helix, which effectively disrupted condensates and impaired T6SS assembly. Comparative analyses of more than 10,000 *V. cholerae fha* sequences reveal strict conservation of the internal start site and its upstream ribosomal binding sequence, indicating strong selective pressure for this strategy across *V. cholerae*. Similar tandem translation was validated not only in a panel of *V. cholerae* strains but also across other *Vibrio* species. By integrating gene-in-gene translation with phase separation, *V. cholerae* has evolved a unique means to control T6SS activities, a mechanism not observed in prior regulatory modules but key for promoting survival, spread, and virulence of *V. cholerae*. These findings reveal a translational–biophysical mechanism for controlling a conserved bacterial contractile machine and suggests a broader evolutionary principle that parallels with eukaryotic systems.

Results

Intragenic coding of *fha* produces two isoforms, Fha^{L} and Fha^{S}

Fha is essential for T6SS activity in *V. cholerae*, but its mechanism remains poorly understood [23]. During purification of C-terminally His-tagged Fha expressed in *E. coli*, we consistently observed two distinct products: a full-length protein and a shorter variant (Fig. 1a). N-terminal Edman sequencing of the smaller product identified methionine 262 as the initiation site, indicating internal translation from an in-frame start codon. To confirm this, we generated an fha^{M262A} mutant, which produced only the full-length isoform (Fig. 1a). In parallel, N-terminal FLAG and C-terminal His tagging showed that FLAG immunoblotting detected only the full-length product, whereas His immunoblotting detected both; both tags detected only the full-length protein in the M262A mutant (Supplementary Fig. 1a). Mutation of the predicted ribosome-binding site upstream of M262 (fha^{E258A}) likewise abolished the shorter isoform, further supporting its translational origin (Supplementary Fig. 1b). We therefore designate the full-length isoform as Fha^{L}, the internally initiated shorter isoform as Fha^{S} (Fig. 1b).

We next validated isoform expression in *V. cholerae* T6SS-model strain V52. Plasmid-borne 3V5-tagged *fha* expressed in a Δ*fha* mutant of strain V52 produced both isoforms, whereas the M262A and E258A variants produced only Fha^{L} (Fig. 1c). To test expression under native conditions, we constructed *fha_sfGFP* fusions at the chromosomal locus. Chromosomal point mutants confirmed isoform identity: the fha^{L} allele (M262A) expressed only the full-length GFP-tagged isoform, whereas the fha^{S} allele (M1A) expressed only the shorter isoform (Fig. 1d).

Finally, we asked whether isoform production occurs in other *V. cholerae* strains. Using polyclonal antisera against Fha, we detected both long and short isoforms in the seventh-pandemic El Tor O1 strain C6706 expressing a plasmid-borne T6SS-activating regulator QstR [24]. As

84 expected, M262A and M1A variants in this background expressed only the full-length or the
85 shorter isoform, respectively (Fig. 1e).

86 Together, these results demonstrate that *V. cholerae fha* generates two isoforms by
87 intragenic translation, establishing the first example of an in-frame gene-in-gene coding strategy
88 in *V. cholerae*.

89 **Long and short isoforms partition initiation and enhancement of T6SS assembly**

90 To define the role of Fha and its isoforms in T6SS biogenesis, we visualized
91 chromosomally tagged Fha_sfGFP together with mCherry2-labeled sheath protein TssB.
92 Fluorescence microscopy revealed discrete cytoplasmic foci that consistently formed at the
93 initiating site of sheath polymerization (Fig. 2a). Fha foci formation was unaltered in Δ*tssM*, Δ*tssA*,
94 and Δ*tssE* mutants defective in T6SS assembly (Supplementary Fig. 1c). Additionally, assemblies
95 of the membrane complex protein TssL_sfGFP and the baseplate protein sfGFP_TssG were
96 undetectable in the absence of Fha (Fig. 2b and c). These results confirm Fha as a key initiator of
97 T6SS assembly in *V. cholerae*.

98 To dissect isoform contributions, we constructed chromosomal mutants expressing only
99 Fha^{L}, Fha^{S}, or Fha^{N} (the N-terminus, residues 1–261), each fused to sfGFP in the background of
100 TssB_mCherry2. Fha^{L} and Fha^{S} each formed fluorescent foci, whereas Fha^{N} was diffuse (Fig. 2d,
101 Supplementary Fig. 1d). Quantification showed that the Fha^{L}-only strain produced initiation foci
102 that colocalized with sheaths but at substantially reduced numbers relative to wild type, whereas
103 the Fha^{S}-only strain failed to initiate sheath assembly (Fig. 2d and e). Notably, the Fha^{N}-only strain
104 produced a slightly reduced number of sheath assembly to the Fha^{L}-only strain (Fig. 2d and e).

105 We next examined functional effects. The fha^{S} mutant (lacking Fha^{L}) exhibited a complete
106 loss of Hcp secretion and killing against *E. coli*, while the fha^{L} and fha^{N} mutants retained

significantly reduced but detectable activity (Fig. 2f and g, Supplementary Fig. 1e). To provide further support, we performed complementation analysis. Wild-type Fha restored Hcp secretion and antibacterial activity in the Δ*fha* mutant, Fha^{L} provided partial rescue, and Fha^{N} yielded low yet detectable recovery (Fig. 2h and i, Supplementary Fig. 1f). In contrast, Fha^{S} alone failed to restore T6SS activity (Fig. 2h and i, Supplementary Fig. 1f).

Together, these data demonstrate that Fha^{L} (containing the N-terminal domain) is sufficient to support a basal level of assembly while Fha^{S} enhances secretion and killing. The presence of both isoforms is necessary for a fully competent T6SS.

The C-terminal domain drives phase separation and isoform cooperation

The punctate localization of Fha suggested a condensate-based assembly. Using a *lacO*-repeat array[25], we estimated that individual Fha foci contain between 80-2500 Fha molecules in *V. cholerae* cells, consistent with biomolecular clustering (Supplementary Fig. 1g and h). Purified Fha^{L} and Fha^{S} each formed oil-like droplets *in vitro* in a concentration-dependent manner, whereas Fha^{N} did not (Fig. 3a, Supplementary Fig. 2a). Pull-down and bacterial two-hybrid assays showed direct interactions between Fha^{L} and Fha^{S} but not between Fha^{N} and either isoform (Fig. 3b, Supplementary Fig. 2b). *In vivo*, plasmid-borne expression of wild-type Fha enhanced Hcp secretion in an fha^{N} mutant background, whereas expression of Fha^{S} alone did not (Supplementary Fig. 2c). Notably, Fha^{S} was shown to partially complement the T6SS activities of fha^{L} mutant (Supplementary Fig. 2d). Together with the observations that Fha^{N}_sfGFP was diffuse *in vivo*, these results indicate that the C-terminal domain is essential for LLPS.

L341 is a key residue required for Fha condensate formation

To mechanistically determine the role of phase separation in T6SS control, we searched for LLPS-defective point mutations within the C-terminal region. Structural modeling revealed a

leucine-rich helix spanning residues from M320 to E350 (Supplementary Fig. 3a). Individual leucine to alanine substitutions identified L341A and L342A as strong LLPS-disrupting mutations, as plasmid-expressed Fha^{L341A}_sfGFP or Fha^{L342A}_sfGFP displayed diffuse cytoplasmic distribution in the V52 Δ*fha* strain (Supplementary Fig. 3b). We further introduced the chromosomal fha^{L341A} mutation into the *fha_sfGFP tssB_mCherry2* background, which did not affect the expression of Fha^{L} and Fha^{S} (Supplementary Fig. 3c). This mutation abolished Fha foci, reduced the number of TssL and TssG foci, and markedly impaired sheath assembly (Fig. 3c, Supplementary Fig. 3 d and e).

Functionally, the fha^{L341A} mutant exhibited severe defects in Hcp secretion and interbacterial competition, both of which were fully rescued by plasmid-borne wild-type Fha (Fig. 3d, e; Supplementary Fig. 3f). Moreover, inducible expression of Fha^{L341A}_sfGFP in the V52 *fha_sfGFP* strain caused pre-existing Fha_sfGFP foci to gradually dissolve, whereas expression of sfGFP or wild-type Fha_sfGFP had no such effect (Supplementary Fig. 3g), indicating that L341A acts as a dominant negative disruptor of condensate integrity.

Design of Fha-leucine-rich-helix-targeting binders using fold-conditioned RFdiffusion

Although the L341A substitution effectively disrupted Fha condensate formation, this mutation alters the primary sequence of Fha and could introduce unintended structural or regulatory effects beyond perturbation of the helix interface. To independently test whether the leucine-rich helix is intrinsically required for condensation, we developed an orthogonal strategy to selectively target this helix without modifying the helix sequence, by using a fold-conditioned RFdiffusion-ProteinMPNN workflow to generate *de novo* protein binders (Fig. 3f) [20]. Guided by our mutational analysis identifying L341, L342 and L334 as critical for condensate formation, these three hydrophobic residues were designated as hotspot positions to promote the formation of

a shape-complementary binding interface. Our analysis generated 12,000 candidate binder sequences (Supplementary data 1), which were subsequently evaluated using AlphaFold2 initial-guess models and ranked based on interface confidence metrics, including high structural confidence and low predicted alignment error at the interface. Ten designs that consistently met these criteria were selected for experimental characterization in *V. cholerae* V52 (Supplementary Fig. 4, Supplementary data 2).

Designed binders impair the formation of Fha condensates and T6SS assembly *in vivo*

Each binder was expressed from an arabinose-inducible plasmid in V52 *fha_sfGFP tssB_mCherry2* strains, allowing simultaneous imaging of Fha condensates and sheath assembly. All ten binders reduced the number of Fha foci to varying degrees, and the magnitude of condensate disruption correlated with a proportional reduction in sheath assembly frequency (Fig. 3g and h, Supplementary Fig. 5a-c). Among the designs, Binder7 exhibited the strongest effect, resulting in predominantly diffuse Fha signals and significantly reduced number of sheath structures, indicating impaired T6SS activities (Fig. 3g and h, Supplementary Fig. 5a-c). This is further confirmed by Hcp secretion that was reduced by Binder7 expression (Fig. 3i). Notably, expression of Binder7 in the fha^{L341A} mutant, which is already defective in condensate formation, did not further decrease Hcp secretion (Fig. 3i). Consistent with these observations, Binder7, but not Binder4 or Binder5, impaired Fha foci formation in *E. coli*, resulting in diffuse cytoplasmic localization of Fha_sfGFP (Supplementary Fig. 5d). Western blotting analysis confirmed that Fha_sfGFP protein levels were comparable across strains expressing different Binders (Supplementary Fig. 5e), indicating that the observed differences in localization reflect condensate disruption rather than altered protein abundance. These data demonstrate that targeted perturbation of the helix interface is sufficient to disrupt Fha condensates and impair T6SS assembly.

Isoforms exhibit distinct recruitment for membrane and baseplate components

The observation that chromosomally tagged Fha localized to the base of extending sheaths suggest its association with the T6SS apparatus. Mass spectrometry of Strep-tagged Fha complexes identified multiple interacting components, including the inner membrane proteins TssL and TssM, baseplate proteins TssA, TssF, and TssK, the secreted effectors VasX and TseL, and the ATPase ClpV (Supplementary Fig. 6a). Domain mapping revealed that Fha^{L} and Fha^{N} interacted strongly with TssL but weakly with TssE, whereas Fha^{S} exhibited the opposite pattern (Fig. 3j). Bacterial two-hybrid assays confirmed that Fha^{L} and Fha^{N} bound the cytoplasmic domain of TssL, while Fha^{S} did not (Supplementary Fig. 6b). Additionally, pull-down assays showed that Fha^{L341A} interacts with TssL and TssE at levels comparable to wild-type Fha (Supplementary Fig. 6c), indicating that the L341A substitution does not disrupt these key T6SS protein–protein interactions even though it abolishes phase separation.

To test the functional significance of these differences, we reconstituted droplet recruitment *in vitro*. GFP-tagged $TssL_{cyto}$ (the cytoplasmic domain of TssL) partitioned efficiently into Fha^{L} droplets but less into Fha^{S} droplets (Supplementary Fig. 6 d and e). Control MBP_sfGFP was excluded from Fha^{L} droplets but weakly enriched in Fha^{S} droplets, indicating distinct selectivity (Supplementary Fig. 6 d and e).

Together, these results demonstrate that the C-terminal domain of Fha mediates phase separation, that this property is crucial for T6SS function, and that isoforms partition their interactions with T6SS components. Fha^{L} anchors to membrane partners such as TssL, whereas Fha^{S} engages baseplate proteins such as TssE, providing a molecular basis for their functional cooperation.

Dual-isoform cooperation enhances survival and colonization in competitive environments

We next evaluated the ecological significance of isoform cooperation. In interbacterial competition, the *fha*^{L} mutant (expressing only Fha^{L}) displayed significantly reduced survival against environmental *V. cholerae*, *V. parahaemolyticus*, and *Aeromonas dhakensis* (Fig. 4a–c, Supplementary Fig. 7a–c). In interactions with eukaryotic predators, the *fha*^{L} mutant was more susceptible to amoeba, and in a murine colonization model it exhibited markedly reduced intestinal loads compared with wild type (Fig. 4d and e). These results demonstrate that Fha^{S} provides a measurable advantage in bacterial competition, predator resistance, and host colonization.

Gene-in-gene coding is evolutionarily conserved across *Vibrio* species

Given the broad ecological benefits of isoform cooperation, we next examined whether this system is preserved by evolutionary selection. Comparative analysis of more than 10,000 *V. cholerae fha* sequences using per-site Shannon entropy revealed absolute conservation of the internal initiation codon (M262) and its ribosome-binding site and the key residue for LLPS (L341), in contrast to normal levels of variation observed across the rest of the *fha* gene (Fig. 5a). Isoform production was experimentally confirmed in a panel of clinical and environmental *V. cholerae* isolates (Fig. 5b). Extending this analysis across the genus, heterologously expressed *fha* homologs from *V. fluvialis*, *V. vulnificus*, and *V. anguillarum* each produced full-length and internally initiated isoforms, which were eliminated by mutation of the internal start codon (Fig. 5c). Additionally, to validate the functions of these isoforms, we constructed a chromosomal *fha_sfGFP* fusion in *V. anguillarum* strain MHK3 and confirmed both isoforms by Western blotting analysis (Fig. 5d). Both the long and short isoforms of Fha are required for full T6SS activity, as chromosomal mutations M1A and M263A, which produce only the short or long isoform respectively, significantly reduced T6SS activities in bacterial competition and Hcp secretion assays (Fig. 5d and e, Supplementary Fig. 7d). Together, these data demonstrate that the

dual-isoform system is ecologically advantageous and has been conserved across *Vibrio* by strong selection.

Discussion

Bacteria deploy sophisticated protein secretion machines whose functional complexity rivals that of many eukaryotic systems. The T6SS exemplifies this sophistication because it builds a cell-spanning contractile apparatus that can physically penetrate Gram-negative, Gram-positive, and even fungal cell envelopes [26-30]. Despite the importance of such machines, most known regulatory paradigms emphasize transcriptional control, while much less is understood about how bacteria fine-tune assembly and activity once the components are already present in the cytosol. This gap is particularly critical for studying bacterial pathogens, which must rapidly activate secretion systems to survive highly fluctuating environmental and host-associated pressures. Here, we reveal a translational–biophysical regulatory mechanism that coordinates T6SS assembly. We show that *V. cholerae* uses intragenic coding to generate two isoforms of the scaffold Fha and that cooperate to regulate the T6SS activity (Fig. 6). The full-length isoform Fha^{L} nucleates assembly by engaging membrane-associated components, whereas the shorter isoform Fha^{S} enhances secretion efficiency through interaction with baseplate proteins and formation of condensates. This division of labor provides a mechanistic explanation for how a single scaffold coordinates the spatial and temporal dynamics of T6SS assembly.

Our data establish a direct mechanistic link between phase separation and T6SS efficiency. Both Fha^{L} and Fha^{S} form liquid-like condensates, and a single leucine-to-alanine substitution (L341A) within a conserved C-terminal α-helix disrupts condensate formation and diminishes T6SS activities. The dominant-negative activity of Fha^{L341A} further supports condensate properties.

Consistently, AI-designed binders targeting this helix also disrupted Fha condensates and impaired T6SS assembly *in vivo*. While secondary effects on Fha interactions cannot be ruled out, these results provide two orthogonal means to strongly support condensate formation as an organizing principle for T6SS assembly and illustrate the utility of computational binder design as a complementary tool for modulating T6SS or other condensate-mediated protein machine assemblies.

How has *V. cholerae* evolved into one of the world's most successful human pathogens? By integrating isoform diversity with condensate-mediated assembly, *V. cholerae* expands its regulatory toolkit beyond canonical transcriptional and post-translational control to promote the efficiency of a complex secretion system that is crucial for survival and virulence. The strict conservation of the internal initiation codon and upstream ribosome-binding site across *V. cholerae* genomes, coupled with the detection of dual isoforms in diverse *Vibrio* species, suggests that dual-isoform cooperation is not a recent innovation but rather an evolutionarily maintained solution for tuning the T6SS assembly.

Despite the mechanistic advances presented here, several limitations remain. First, while Fha condensates are clearly crucial for T6SS activity, the biophysical determinants of condensate stability and dynamics are not fully resolved. We do not yet understand whether material properties (such as viscosity, turnover rates, or maturation state) change during the T6SS assembly cycle or in response to physiological cues, particularly under nutrient limitation or other stresses. Second, because Fha interacts with but substantially outnumbers inner-membrane T6SS components [31], it is plausible that cytosolic Fha may function as a molecule glue to capture the relatively less-mobile membrane proteins and low abundant cytosolic components and facilitates their incorporation into an initiation site. Within the condensate, initial weak multivalent interactions would transition to

stronger and canonical protein-protein interactions among structural proteins. However, the precise temporal sequence and spatial coordination of these recruitment events remain incompletely defined. Third, to what extent condensate formation influences effector loading and competition is also unclear [32-35]. Future structural, single-molecule, and high-resolution imaging approaches will be required to define how condensates orchestrate the dynamic T6SS process. Finally, although Fha is conserved in many T6SSs and known to be crucial to T6SS functions, not all T6SSs encode an Fha homolog [17,36-39]; whether alternative LLPS regulators exist in these systems, or whether they rely on other mechanisms (such as higher protein expression and spatially restricted localization at the pole) need to be determined.

Together, these findings from *V. cholerae* highlight that bacteria can expand regulatory capacity under genomic constraints by integrating gene-in-gene coding architecture coupled with biophysical control, representing an underappreciated principle of bacterial evolution. This also represents a bacterial parallel to isoform diversification and biomolecular clustering observed in eukaryotic systems, revealing a generalizable strategy for organizing complex molecular machines in compact genomes.

Materials and Methods

Bacterial strains, plasmids, and growth conditions

V. cholerae, *A. dhakensis,* and *E. coli* strains were cultured in LB medium (1% [w/v] tryptone, 0.5% [w/v] yeast extract, and 0.5% [w/v] NaCl), *V. parahaemolyticus* strains were cultured in LB3 medium (1% [w/v] tryptone, 0.5% [w/v] yeast extract, and 3% [w/v] NaCl), while *V. anguillarum* MHK3 strains were cultured in TSB medium (1.7% [w/v] tryptone, 0.3% [w/v] soy peptone, 0.25% [w/v] glucose, 1.5% [w/v] NaCl, and 0.25% [w/v] K_2HPO_4) unless otherwise stated. Antibiotics were supplemented at the following concentrations: streptomycin (100 μg/ml), kanamycin (50 μg/ml), gentamicin (20 μg/ml), and carbenicillin (50 μg/ml). Plasmids were constructed using Gibson assembly and validated by Sanger sequencing. Precise gene deletion mutants were generated via homologous recombination using the pDS132 suicide vector. A comprehensive list of plasmids, strains, and primers used in this study is provided in Supplementary Table 1.

Bacterial competition assay

Killer strains were cultured in liquid medium to the exponential phase, while prey strains were collected from overnight LB-agar plates. For *V. cholerae* interspecies competition, *V. cholerae* V52 was mixed with *E. coli* MG1655 at a 10:1 ratio (LB-agar, 3 h, 37°C), with *A. dhakensis* SSU at 1:10 (LB-agar, 3 h, 37°C), and with *V. parahaemolyticus* RIMD2210633 at 1:10 (LB3-agar, 14 h, 37°C). For *V. cholerae* intraspecies competition, *V. cholerae* V52 was mixed with CH-GX at a 1:10 ratio (LB-agar, 3 h, 37°C). For *V. anguillarum* interspecies competition, *V. anguillarum* MHK3 was mixed with *E. coli* MG1655 at a 10:1 ratio (TSB-agar, 3 h, 28°C). Following incubation, survival was quantified by 10-fold serial dilution on selective media. Error bars represent the mean ± standard deviation from at least three biological replicates. Statistical

significance was assessed using one-way ANOVA with Dunnett's multiple comparisons test or Student's *t*-test in GraphPad Prism (version 10.1.2).

Fluorescence microscopy of T6SS assembly

Strains were grown in LB medium to an OD_{600} of ~1. Cultures were centrifuged at 4,500 × g for 2 min, resuspended in LB medium to an OD_{600} of ~10, and spotted onto 1% agarose–0.5× PBS pads for imaging. Fluorescence microscopy was performed using a Nikon Ti-E A1R HD25+ SIM S microscope, equipped with the Perfect Focus System, a CFI SR HP Apochromat TIRF 100×C objective lens (NA 1.49), and 488/561 nm excitation lasers. For Fig. 3c, Supplementary Fig. 3, and Supplementary Fig. 5, an Olympus IX85 Inverted microscope was used, featuring the 100× oil objective lens (NA 1.5). GFP and mCherry filter sets were used for fluorescence excitation. All imaging experiments were performed at least twice, with representative results shown.

Protein purification

Strep-tagII-tagged or His-tagged proteins were expressed in *E. coli* BL21(DE3) using pET vectors. Cultures were grown in LB medium to an OD_{600} of ~0.5 at 37°C, followed by induction with 1 mM IPTG at 16°C for 16 h. Cells were harvested by centrifugation at 4,500 × g for 15 min. For the purification of Strep-tagII-tagged proteins, the pellets were resuspended in PBS buffer (10 mM Na_2HPO_4, 140 mM NaCl, 3 mM KCl, pH 7.4) and lysed by sonication. The lysates were clarified by centrifugation at 15,000 × g for 30 min, and the resulting supernatants were incubated with Streptactin beads (Smart-lifesciences). Bound proteins were eluted with PBS containing 2.5 mM biotin. For the purification of His-tagged proteins, pellets were resuspended in Tris buffer (20 mM Tris-HCl, 150 mM NaCl, pH 7.4) and subjected to sonication. Lysates were centrifuged at 15,000 × g for 30 min, and the supernatants were incubated with Ni-NTA beads (Smart-lifesciences). Proteins were subsequently eluted with Tris buffer containing varying concentrations of imidazole.

In vitro liquid–liquid phase separation (LLPS) assay

Purified proteins were dialyzed against LLPS buffer (10 mM Na_2HPO_4/NaH_2PO_4, 200 mM NaCl, pH 7.4) and concentrated using centrifugal filter units equipped with Ultracel-10K membranes to a final concentration of approximately 80 μM. The concentrated proteins were subjected to 2-fold serial dilution in LLPS buffer and subsequently mixed 1:1 with 20% dextran-70 prepared in the same buffer, unless otherwise specified. The mixtures were immediately loaded onto glass slides for imaging. Imaging was performed using a ZEISS LSM 980 with Airyscan 2 microscope fitted with a 63×/1.40 oil objective and a 488 nm laser. All imaging experiments were repeated at least twice, and representative images are shown.

Western blotting analysis

Proteins were separated via SDS-PAGE (Yeasen Biotechnology) and transferred to a PVDF membrane (Bio-Rad). Membranes were blocked with 5% (w/v) non-fat milk in TBST (50 mM Tris, 150 mM NaCl, 0.1% [v/v] Tween-20, pH 7.6) for 1 h at room temperature, followed by incubation with primary antibodies and HRP-conjugated secondary antibodies in 1% (w/v) non-fat milk in TBST. Signal detection was carried out using Clarity ECL reagent (Bio-Rad). Monoclonal antibodies against FLAG (#SLAB0102) and 6×His (#SLAB2803) were obtained from Smart-lifesciences, V5 (#AE017) was ordered from ABclonal, and RpoB (#663905) was purchased from BioLegend. The polyclonal anti-Hcp and anti-Fha antibodies were custom-generated by Shanghai Youlong Biotech. HRP-linked secondary antibodies were acquired from ZSGB-Bio (#ZB-2305 [mouse] and #ZB-2301 [rabbit]).

Protein pull-down assay

Epitope-tagged constructs were generated by cloning genes of interest into pET, pBAD, and pBBR1MCS2 vectors as specified. For protein expression, *E. coli* BL21(DE3) carrying pET

plasmids was grown in LB medium to OD_{600} ~0.6 at 37°C and induced with 1 mM IPTG overnight at 20°C. *E. coli* T-Fast carrying pBAD plasmids was grown under similar conditions and induced with 0.1% arabinose for 3 h at 30°C. For pBBR1MCS2, *E. coli* T-Fast cultures were grown in LB for ~6 h at 37°C. Cells were harvested by centrifugation, resuspended in lysis buffer (20 mM Tris, 500 mM NaCl, 50 mM imidazole, 1× protease inhibitor [Thermo Scientific], pH 8.0), and subjected to sonication on ice for lysis. After centrifugation, supernatants were incubated with Ni-NTA beads (Smart-lifesciences) for 1 h at 4°C with rotation. Beads were washed four times with wash buffer (20 mM Tris, 500 mM NaCl, 50 mM imidazole, pH 8.0) and eluted with elution buffer (20 mM Tris, 500 mM NaCl, 400 mM imidazole, pH 8.0). Input and eluate samples were analyzed by Western blotting. For pull-down experiments in *V. cholerae* V52, Strep-tagII-tagged Fha and sfGFP were enriched from cell lysates using Streptactin beads (Smart-lifesciences). Bound proteins were analyzed via LC-MS/MS at Jingjie PTM BioLab.

Protein secretion assay

For *V. cholerae* V52 strains, cultures were grown in LB with appropriate antibiotics at 30 °C to OD_{600} = 1.0 and collected by centrifugation at 2,500 × g for 8 min. Pellets were resuspended in fresh LB and incubated at 30 °C for 2 h with or without 0.01% (w/v) L-arabinose. For experiments shown in Fig. 3i, to induce binder expression in V52, 0.1% (w/v) L-arabinose was included both during culture growth and the subsequent static induction period. Cultures were centrifuged twice at 10,000 × g for 2 min to separate pellets and supernatants. Both fractions were mixed with SDS-loading buffer and defined as “Cell” and “Sec” samples, respectively. For *V. anguillarum* MHK3 strains, cultures were grown in TSB with appropriate antibiotics at 28 °C to OD_{600} = 1.0 and collected by centrifugation at 2,500 × g for 8 min. Pellets were resuspended in fresh TSB and incubated at 28 °C for 2 h. Cells were pelleted at 10,000 × g for 2 min and resuspended in SDS-

loading buffer as "Cell" samples. Supernatants were clarified again, precipitated with 20% (v/v) TCA at −20 °C for 20 min, centrifuged at 15,000 × g for 30 min at 4 °C, washed twice with acetone, air-dried, and resuspended in SDS-loading buffer. All samples were boiled for 10 min before SDS-PAGE analysis.

Fluorescence quantification

Fluorescence measurements were carried out following a previously published protocol [25]. The *lacO* array was engineered to contain repeated operator sequences separated by 18-nucleotide randomized spacers. A mutant variant of LacI ($LacI^{mut}$), which lacks the C-terminal tetramerization domain but preserves DNA-binding affinity comparable to wild-type LacI, was fused to sfGFP and used to calibrate the sfGFP molecule number required to generate detectable foci of defined intensity in cells. $LacI^{mut}$_sfGFP was expressed from the pBAD24 plasmid and induced with 0.002% L-arabinose in V52 strains harboring different numbers of integrated *lacO* repeats. Fluorescence signals from LacI and Fha foci were extracted in Fiji, and all quantifications were performed on unprocessed images.

Bacterial two-hybrid assay

Proteins of interest were fused to the T18 and T25 fragments of *Bordetella adenylate* cyclase [40]. Plasmids encoding the fusion proteins were co-transformed into the reporter strain BTH101. Three independent colonies per transformation were grown in 500 µl LB at 37 °C for 5 h. Three microliters of each culture were then spotted onto LB plates containing ampicillin, kanamycin, IPTG (0.04 mM), and X-Gal (80 µg/ml), followed by incubation for 6 h at 30 °C and an additional 10 h at room temperature. Experiments were performed in triplicate, and a representative result is shown.

Amoeba plaque assay

V. cholerae V52 cultures were grown overnight at 37°C, harvested by centrifugation (10,000 × g, 1 min), and resuspended in 1 ml PBS. A 100-µl aliquot of bacterial suspension was spread onto SM/5 plates and air-dried at room temperature. *D. discoideum* cells were collected from SM/5 plates containing WM6026, pelleted by centrifugation (500 × g, 4 min), washed five times with PBS, and resuspended to ~1.5×10^7 cells/ml. Serial five-fold dilutions of amoebae were spotted onto SM/5 plates pre-seeded with bacteria. Plates were incubated at 22°C for 3–7 days, after which plaque formation was assessed. The minimal number of *D. discoideum* cells capable of forming plaques on the bacterial lawn was recorded.

Infant mouse infections

Infant mouse infections were performed as previously described [41]. Five-day-old CD1 mice were weaned for 2–3 h before oral inoculation with *V. cholerae* V52 (5×10^9 CFU) and maintained at 30°C for 16–18 h. Small intestines were then harvested, homogenized, and plated to quantify bacterial colonization.

Binder protein sequence design

De novo binders were designed using a fold-conditioned RFdiffusion–ProteinMPNN workflow. The AlphaFold2-predicted structure of the Fha leucine-rich helix was used as the conditioning input to guide scaffold generation. RFdiffusion was used to generate 4,000 initial scaffolds with geometries compatible with helix engagement. L334, L341, and L342 were specified as hotspot positions during the diffusion process to promote the formation of a shape-complementary binding interface. Sequence optimization of the resulting scaffolds was performed using ProteinMPNN with amino-acid–biased sampling, yielding a total of 12,000 candidate sequences (Supplementary Data 1). Structural evaluation of the designs was carried out using AlphaFold2 initial-guess models. Designs were filtered based on multiple confidence metrics, including high per-residue structural

confidence (pLDDT > 0.9), high interface predicted TM-score (i_pTM > 0.85), and low interface predicted alignment error (i_PAE < 5 Å). Ten designs that consistently met these criteria were selected for experimental characterization (Supplementary Data 2).

Bioinformatic analysis

All gene sequences of *V. cholerae* V52 were retrieved from the draft genome assembly (GenBank NC_002505.1 and NC_002506.1), managed and analyzed by Benchling. For comparative analysis of *V. cholerae fha* sequences using per-site Shannon entropy in Fig. 5a, *V. cholerae* genomes (n = 10,117) were downloaded from NCBI and annotated with Prokka to obtain protein (.faa) and CDS (.ffn) files. Full-length Fha proteins were retrieved by BLASTx (coverage >99%) against the .faa files (10,026 sequences) and aligned with MAFFT. CDS sequences were then threaded onto the protein alignment to maintain codon-level correspondence (Supplementary data 3). Alignments were truncated to 495 amino acids based on the V52 Fha reference, and per-site Shannon entropy was calculated at the nucleotide level as $H = -\sum_i p_i log_2 p_i$, where p_i is the frequency of each nucleotide at a given codon position.

Acknowledgments

This work was supported by funding from National Natural Science Foundation of China (32500088, W2431022, W2433062, 32400096, 32530004), and China Postdoctoral Science Foundation (2025M782655 and GZC20251798). The funders had no role in study design, data collection, and interpretation, or the decision to submit the work for publication. We thank Dr. Zhaolan Mo from the Yellow Sea Fisheries Research Institute, Chinese Academy of Fishery Sciences, for generously providing the *V. anguillarum* MHK3 strain. We also thank Dr. Haiwei Luo from The Chinese University of Hong Kong for technical assistance.

Author contributions

T.D. conceived the project. T.P., Q.C., X.W., J.L., Z.Y., Y.L., J.S., X.L., and Y.A. performed bacterial research and provided key resources. A.M. and J.Z. performed mouse infection. T.P. and T.D. wrote the manuscript.

Conflict of interests

The authors declare no competing interests.

References

1 Neeves, J. *et al.* An alternative cytoplasmic SFPQ isoform with reduced phase separation potential is up-regulated in ALS. *Sci Adv* **11**, eadt4814 (2025). https://doi.org/10.1126/sciadv.adt4814

2 Batlle, C. *et al.* hnRNPDL Phase Separation Is Regulated by Alternative Splicing and Disease-Causing Mutations Accelerate Its Aggregation. *Cell Rep* **30**, 1117-1128 e1115 (2020). https://doi.org/10.1016/j.celrep.2019.12.080

3 Liu, B. & Abdel-Wahab, O. Oncogenic splicing regulated by phase separation. *Nat Cell Biol* **22**, 916-918 (2020). https://doi.org/10.1038/s41556-020-0553-5

4 Huvet, M. & Stumpf, M. P. Overlapping genes: a window on gene evolvability. *BMC Genomics* **15**, 721 (2014). https://doi.org/10.1186/1471-2164-15-721

5 Wright, B. W., Molloy, M. P. & Jaschke, P. R. Overlapping genes in natural and engineered genomes. *Nat Rev Genet* **23**, 154-168 (2022). https://doi.org/10.1038/s41576-021-00417-w

6 Meydan, S., Vazquez-Laslop, N. & Mankin, A. S. Genes within Genes in Bacterial Genomes. *Microbiol Spectr* **6** (2018). https://doi.org/10.1128/microbiolspec.RWR-0020-2018

7 Yu, X. J., Liu, M., Matthews, S. & Holden, D. W. Tandem translation generates a chaperone for the Salmonella type III secretion system protein SsaQ. *J Biol Chem* **286**, 36098-36107 (2011). https://doi.org/10.1074/jbc.M111.278663

8 Baker-Austin, C. *et al.* Vibrio spp. infections. *Nat Rev Dis Primers* **4**, 8 (2018). https://doi.org/10.1038/s41572-018-0005-8

9 Mekalanos, J. J. in *Epidemiological and Molecular Aspects on Cholera* (eds T. Ramamurthy & S. K. Bhattacharya) 97-114 (Springer New York, 2011).

10 Kanungo, S., Azman, A. S., Ramamurthy, T., Deen, J. & Dutta, S. Cholera. *Lancet* **399**, 1429-1440 (2022). https://doi.org/10.1016/S0140-6736(22)00330-0

11 Pukatzki, S. *et al.* Identification of a conserved bacterial protein secretion system in *Vibrio cholerae* using the *Dictyostelium* host model system. *Proceedings of the National Academy of Sciences of the United States of America* **103**, 1528-1533 (2006). https://doi.org/10.1073/pnas.0510322103

12 Basler, M., Pilhofer, M., Henderson, G. P., Jensen, G. J. & Mekalanos, J. J. Type VI secretion requires a dynamic contractile phage tail-like structure. *Nature* **483**, 182-186 (2012). https://doi.org/10.1038/nature10846

13 Dong, T. G., Ho, B. T., Yoder-Himes, D. R. & Mekalanos, J. J. Identification of T6SS-dependent effector and immunity proteins by Tn-seq in *Vibrio cholerae*. *Proceedings of the National Academy of Sciences of the United States of America* **110**, 2623-2628 (2013). https://doi.org/10.1073/pnas.1222783110

14 Pukatzki, S., Ma, A. T., Revel, A. T., Sturtevant, D. & Mekalanos, J. J. Type VI secretion system translocates a phage tail spike-like protein into target cells where it cross-links actin. *Proceedings of the National Academy of Sciences of the United States of America* **104**, 15508-15513 (2007). https://doi.org/10.1073/pnas.0706532104

15 Wang, J., Brodmann, M. & Basler, M. Assembly and subcellular localization of bacterial type VI secretion systems. *Annual Review of Microbiology* **73**, 621-638 (2019). https://doi.org/10.1146/annurev-micro-020518-115420

16 Ho, B. T., Dong, T. G. & Mekalanos, J. J. A view to a kill: the bacterialtype VI secretion system. *Cell Host & Microbe* **15**, 9-21 (2014). https://doi.org/10.1016/j.chom.2013.11.008

17 Pei, T. T. *et al.* Fha initiates the inside-out assembly of the type VI secretion system. *Cell Rep* **44**, 115990 (2025). https://doi.org/10.1016/j.celrep.2025.115990

18 Pei, T. T. *et al.* TssW-PpkA-Fha axis controls the positioning and initiation of the type VI secretion system in *Acidovorax citrulli*. *mBio*, e0187925 (2025). https://doi.org/10.1128/mbio.01879-25

19 Watson, J. L. *et al.* De novo design of protein structure and function with RFdiffusion. *Nature* **620**, 1089-1100 (2023). https://doi.org/10.1038/s41586-023-06415-8

20 Vazquez Torres, S. *et al.* De novo design of high-affinity binders of bioactive helical peptides. *Nature* **626**, 435-442 (2024). https://doi.org/10.1038/s41586-023-06953-1

21 Dauparas, J. *et al.* Robust deep learning-based protein sequence design using ProteinMPNN. *Science* **378**, 49-56 (2022). https://doi.org/10.1126/science.add2187

22 Sun, G. *et al.* De novo design of protein binders to stabilize monomeric TDP-43 and inhibit its pathological aggregation. *Proc Natl Acad Sci U S A* **122**, e2505320122 (2025). https://doi.org/10.1073/pnas.2505320122

23 Zheng, J., Ho, B. & Mekalanos, J. J. Genetic analysis of anti-amoebae and anti-bacterial activities of the type VI secretion system in *Vibrio cholerae*. *PloS One* **6**, e23876-e23876 (2011). https://doi.org/10.1371/journal.pone.0023876

24 Jaskolska, M., Stutzmann, S., Stoudmann, C. & Blokesch, M. QstR-dependent regulation of natural competence and type VI secretion in *Vibrio cholerae*. *Nucleic Acids Res* **46**, 10619-10634 (2018). https://doi.org/10.1093/nar/gky717

25 Schneider, J. P. *et al.* Diverse roles of TssA-like proteins in the assembly of bacterial type VI secretion systems. *The EMBO Journal* **38**, 1-17 (2019). https://doi.org/10.15252/embj.2018100825

26 Pei, T. T. *et al.* Delivery of an Rhs-family nuclease effector reveals direct penetration of the gram-positive cell envelope by a type VI secretion system in *Acidovorax citrulli*. *mLife* **1**, 66-78 (2022). https://doi.org/10.1002/mlf2.12007

27 Hood, R. D. *et al.* A type VI secretion system of *Pseudomonas aeruginosa* targets a toxin to bacteria. *Cell Host & Microbe* **7**, 25-37 (2010). https://doi.org/10.1016/j.chom.2009.12.007

28 Trunk, K. *et al.* The type VI secretion system deploys antifungal effectors against microbial competitors. *Nature Microbiology* **3**, 920-931 (2018). https://doi.org/10.1038/s41564-018-0191-x

29 Le, N. H., Pinedo, V., Lopez, J., Cava, F. & Feldman, M. F. Killing of Gram-negative and Gram-positive bacteria by a bifunctional cell wall-targeting T6SS effector. *Proceedings of the National Academy of Sciences of the United States of America* **118**, 6-11 (2021). https://doi.org/10.1073/pnas.2106555118

30 MacIntyre, D. L., Miyata, S. T., Kitaoka, M. & Pukatzki, S. The *Vibrio cholerae* type VI secretion system displays antimicrobial properties. *Proceedings of the National Academy of Sciences of the United States of America* **107**, 19520-19524 (2010). https://doi.org/10.1073/pnas.1012931107

31 Lin, L., Lezan, E., Schmidt, A. & Basler, M. Abundance of bacterial Type VI secretion system components measured by targeted proteomics. *Nature Communications* **10**, 2584-2584 (2019). https://doi.org/10.1038/s41467-019-10466-9

32 Liang, X. *et al.* An onboard checking mechanism ensures effector delivery of the type VI secretion system in *Vibrio cholerae*. *Proceedings of the National Academy of Sciences of the United States of America* **116**, 23292-23298 (2019). https://doi.org/10.1073/pnas.1914202116

33 Burkinshaw, B. J. *et al.* A type VI secretion system effector delivery mechanism dependent on PAAR and a chaperone-co-chaperone complex. *Nature Microbiology* **3** (2018). https://doi.org/10.1038/s41564-018-0144-4

34 Liang, X. *et al.* VgrG-dependent effectors and chaperones modulate the assembly of the type VI secretion system. *PLOS Pathogens* **17**, e1010116-e1010116 (2021). https://doi.org/10.1371/journal.ppat.1010116

35 Wu, C. F. *et al.* Effector loading onto the VgrG carrier activates type VI secretion system assembly. *EMBO reports* **21**, e47961-e47961 (2020). https://doi.org/10.15252/embr.201947961

36 Lin, J.-S. *et al.* Fha interaction with phosphothreonine of TssL activates type VI secretion in Agrobacterium tumefaciens. *PLoS pathogens* **10**, e1003991-e1003991 (2014). https://doi.org/10.1371/journal.ppat.1003991

37 Bingle, L. E. H., Bailey, C. M. & Pallen, M. J. Type VI secretion: a beginner's guide. *Current Opinion in Microbiology* **11**, 3-8 (2008). https://doi.org/10.1016/j.mib.2008.01.006

38 Mougous, J. D., Gifford, C. A., Ramsdell, T. L. & Mekalanos, J. J. Threonine phosphorylation post-translationally regulates protein secretion in Pseudomonas aeruginosa. *Nature Cell Biology* **9**, 797-803 (2007). https://doi.org/10.1038/ncb1605

39 Ostrowski, A. *et al.* Killing with proficiency: Integrated post-translational regulation of an offensive Type VI secretion system. *PLoS Pathogens* **14**, 1-25 (2018). https://doi.org/10.1371/journal.ppat.1007230

40 Karimova, G., Pidoux, J., Ullmann, A. & Ladant, D. A bacterial two-hybrid system based on a reconstituted signal transduction pathway. *Proceedings of the National Academy of Sciences of the United States of America* **95**, 5752-5756 (1998). https://doi.org/10.1073/pnas.95.10.5752

41 Ma, A. T. & Mekalanos, J. J. *In vivo* actin cross-linking induced by *Vibrio cholerae* type VI secretion system is associated with intestinal inflammation. *Proceedings of the National Academy of Sciences of the United States of America* **107**, 4365-4370 (2010). https://doi.org/10.1073/pnas.0915156107

Figure legends

Fig. 1. V52 *fha* gene expresses both the full-length Fha^{L} and a smaller Fha^{S}. A, Comparison of purified Fha and the Fha^{M262A} mutant. C-terminal His-tagged Fha and Fha^{M262A} were expressed and purified with a nickel column. The smaller band in the purified Fha samples was excised for N-terminal Edman sequencing and LC-MS/MS analysis. **B**, Schematic of Fha and its truncated variants. **C**, Western blotting analysis of Fha, Fha^{M262A}, and Fha^{E258A} in V52 Δ*fha* strains. All constructs were cloned to pBAD24 vectors with a C-terminal 3V5 tag. Proteins were induced with 0.01% arabinose at 30℃ for 2 h. **D**, Western blotting analysis of chromosomally encoded Fha in V52 *fha_sfGFP*, *fha^{L}_sfGFP*, and *fha^{S}_sfGFP* strains. **E**, Western blotting analysis of chromosomally encoded Fha in C6706 wild-type, Δ*fha*, *fha^{L}*, and *fha^{S}* strains. Plasmid-borne V5-tagged QstR was expressed to activate T6SS in C6706.

Fig. 2. Both Fha^{L} and Fha^{S} contribute to T6SS function in *V. cholerae* V52. A, Time-lapse images showing co-localization between Fha_sfGFP and TssB_mCherry2 in V52. The white arrow highlights a Fha focus appearing before sheath assembly. The yellow dashed lines outline the T6SS cell. Images were acquired using structured illumination microscopy (SIM). A representative 3 × 3 μm field is shown. Scale bar: 1 μm. Fluorescence images showing TssL_sfGFP (**B**) or sfGFP_TssG (**C**) signals in V52 Parental and Δ*fha*. **D**, Fluorescence images showing co-localization between Fha_sfGFP and TssB_mCherry2 in V52 Parental (*fha_sfGFP tssB_mCherry2*), *fha^{L}*, *fha^{S}*, and *fha^{N}*. For B-D, a representative 5- × 5-μm field of cells is shown. Scale bar: 1 μm. **E**, Quantification of cells forming TssB_mCherry2 foci in Parental (*fha_sfGFP tssB_mCherry2*), *fha^{L}*, and *fha^{N}* strains. The fractions of TssB foci that either co-localize with Fha foci (dark gray) or form in the absence of Fha foci (light gray) are displayed. **F**, Secretion analysis of Hcp in V52 wild-type, T6SS-null mutant Δ*tssM*, *fha_sfGFP*, *fha^{L}_sfGFP*, *fha^{S}_sfGFP*, and *fha^{N}_sfGFP* strains. **G**, Competition analysis of V52 wild-type, T6SS-null mutant Δ*tssM*, *fha_sfGFP*, *fha^{L}_sfGFP*, *fha^{S}_sfGFP*, and *fha^{N}_sfGFP* strains. **H**, Secretion analysis of Hcp in V52 wild-type, T6SS-null mutant Δ*tssM*, Δ*fha*, and Δ*fha* strains expressing plasmid-borne Fha and its variants, as indicated. For F and H, RpoB serves as a control for equal loading and autolysis. **I**, Competition analysis of V52 wild-type, T6SS-null mutant Δ*tssM*, Δ*fha*, and Δ*fha* strains expressing plasmid-borne Fha and its variants, as indicated. For G and I, killer strains are indicated and the prey strain is the *E. coli* MG1655 carrying pPSV37-sfGFP plasmid. Error bars indicate the

mean +/- standard deviation of three biological replicates and statistical significance was calculated using One-way ANOVA test for each group, *$P < 0.05$, **$P < 0.01$, ***$P < 0.001$, ****$P < 0.0001$. DL, detection limit.

Fig. 3. The C-terminal domain of Fha mediates phase separation and facilitates isoform cooperation. A, DIC images showing LLPS of Fha^{L} and Fha^{S} at the indicated concentrations. A representative 30- × 30-μm field of cells is shown. Scale bar: 5 μm. **B**, Interaction of Fha^{L}, Fha^{N}, and Fha^{S} with each other. Pull-down analysis was conducted using His-tagged sfGFP (control), Fha^{L}_sfGFP, Fha^{S}_sfGFP, or Fha^{N}_sfGFP, and FLAG-tagged MBP (control), Fha^{L}, Fha^{S}, or Fha^{N}. **C**, Fluorescence images showing co-localization between Fha_sfGFP and TssB_mCherry2 in V52 Parental (*fha_sfGFP tssB_mCherry2*) and fha^{L341A}. A representative 5- × 5-μm field of cells is shown. Scale bar: 1 μm. **D**, Competition analysis of V52 Parental (*fha_sfGFP*), T6SS-null mutant Δ*tssM*, fha^{L341A} and fha^{L341A} expressing plasmid-borne Fha. Killer strains are indicated and the prey strain is the *E. coli* MG1655 carrying pPSV37-sfGFP plasmid. Error bars indicate the mean +/- standard deviation of three biological replicates. **E**, Secretion analysis of Hcp in V52 Parental (*fha_sfGFP*), T6SS-null mutant Δ*tssM*, fha^{L341A} and fha^{L341A} expressing plasmid-borne Fha. **F**, Design pipeline for Fha leucine-rich helix-targeting binders using fold-conditioned RFdiffusion. Scaffold backbones were generated using 50 RFdiffusion steps with enhanced interface contact potential. ProteinMPNN was then used for sequence optimization, generating three sequences per scaffold, yielding a total of 12,000 binder designs. Binder candidates were evaluated using AlphaFold2 initial-guess predictions and filtered based on multiple confidence metrics, including high per-residue structural confidence (pLDDT > 0.9), high interface predicted TM-score (i_pTM > 0.85), and low interface predicted alignment error (i_PAE < 5 Å). Ten designs that consistently met these criteria were selected for experimental characterization in V52. **G**, Quantification of cells forming Fha_sfGFP foci in V52 Parental (*fha_sfGFP tssB_mCherry2*), fha^{L341A}, and Parental expressing plasmid-borne Binder7. **H**, Quantification of cells forming TssB_mCherry2 foci in V52 Parental (*fha_sfGFP tssB_mCherry2*), fha^{L341A}, and Parental expressing plasmid-borne Binder7. For G and H, each data point represents the number of foci per cell quantified from an individual 30- × 30- μm field of view. **I**, Secretion analysis of Hcp in V52 Parental (*fha_sfGFP tssB_mCherry2*), T6SS-null mutant Δ*fha*, fha^{L341A}, Parental expressing plasmid-borne Binder7, and fha^{L341A} expressing plasmid-borne Binder7. For E and I, RpoB serves as a control for equal

loading and autolysis. **J**, Interaction of Fha^{L}, Fha^{N}, and Fha^{S} with TssL and TssE. Pull-down analysis was conducted using His-tagged sfGFP (control), Fha^{L}_sfGFP, Fha^{S}_sfGFP, or Fha^{N}_sfGFP, and FLAG-tagged MBP (control), TssL, or TssE. Statistical significance was calculated using One-way ANOVA test for each group, ***$P < 0.001$, ****$P < 0.0001$. DL, detection limit.

Fig. 4. Fha^{S} promotes survival and colonization of *V. cholerae* in competitive environments. Competition analysis of the V52 wild-type, T6SS-null mutant Δ*tssM*, and fha^{L} strains against *V. cholerae* strain CH-GX-YL-YZ-T2-3-2021 (abbreviated as VC CH-GX) or V52 (**A**), *V. parahaemolyticus* RIMD2210633 (abbreviated as VP) or its T6SS12-null mutant (ΔT6SS) (**B**), and *A. dhakensis* SSU wild-type or Δ*tssM* strains (**C**). **D**, Competition of V52 wild-type, T6SS-null mutant Δ*tssM*, and fha^{L} strains with the phagocytic *D. discoideum*. The minimal number of amoeba cells to form a plaque is shown in y-axis. **E**, Colonization efficiency of V52 wild-type and fha^{L} strains in the small intestine of infant mice, measured as colony-forming units (c.f.u.) recovered after overnight infection. Error bars represent mean ± standard deviation from at least three independent biological replicates. Statistical significance was determined using one-way ANOVA (for **A**–**D**) or Student's *t*-test (for **E**), *$P < 0.05$, **$P < 0.01$, ***$P < 0.001$, ****$P < 0.0001$.

Fig. 5. Dual isoform expression of Fha homologs is widespread among *Vibrio* species. A, Nucleotide-level entropy landscape of more than 10,000 *V. cholerae fha* alleles. Per-site Shannon entropy was computed to quantify sequence conservation across the *fha* locus. Two sharply conserved regions corresponding to the internal start codon (M262) and the LLPS-associated residue (L341) are indicated, with nucleotide windows 769–792 and 1012–1035 shown in zoomed insets. **B**, Western blotting analysis of chromosomally encoded Fha in different *V. cholerae* strains. **C**, Comparison of purified Fha homologs and their mutants. C-terminal His-tagged proteins were expressed and purified with a nickel column. *V.f.*, *V.v.*, and *V.a.* indicate *V. fluvialis*, *V. vulnificus*, and *V. anguillarum*, respectively. **D**, Secretion analysis of Hcp in *V. anguillarum* MHK3 wild-type, T6SS-null mutant Δ*tssM*, Δ*fha, fha_sfGFP*, fha^{L}*_sfGFP*, fha^{S}*_sfGFP*, and fha^{N}*_sfGFP* strains. RpoB serves as a control for equal loading and autolysis. **E**, Competition analysis of *V. anguillarum* MHK3 wild-type, Δ*fha, fha_sfGFP*, fha^{L}*_sfGFP*, fha^{S}*_sfGFP*, and fha^{N}*_sfGFP*

strains. Killer strains are indicated and the prey strain is the *E. coli* MG1655 carrying pBAD18Kan plasmid. Error bars indicate the mean +/- standard deviation of three biological replicates and statistical significance was calculated using One-way ANOVA test for each group, *$P < 0.05$, ****$P < 0.0001$. DL, detection limit.

Fig. 6. Isoform cooperation of Fha through phase separation promotes *V. cholerae* fitness and pandemic success. A, The *fha* gene produces two isoforms through intragenic translation: the full-length Fha^{L} and the shorter Fha^{S}. The internal start codon is highly conserved without SNPs among over 10,000 *V. cholerae* isolates. **B**, Both Fha^{L} and Fha^{S} undergo liquid–liquid phase separation and selectively recruit essential T6SS components. Through functional partitioning, the isoform condensate enriches structural components and promotes assembly efficiency. **C**, This conserved dual-isoform strategy enables *V. cholerae* with effective intra- and inter- bacterial killing ability, protection against protist predation, and successful host colonization, contributing to ecological fitness and likely spread of cholera disease.

Supplementary Figure 1. Fha^{L} and Fha^{S} contribute to T6SS activities in *V. cholerae* V52. A, Western blotting analysis of Fha and Fha^{M262A}. All constructs were cloned to pET22b vectors with an N-terminal FLAG tag and a C-terminal His tag. Proteins were induced in *E. coli* BL21(DE3) with 1 mM IPTG at 20℃ for 2 h. **B**, Western blotting analysis of Fha and Fha^{E258A}. All constructs were cloned to pBAD24 vectors with a C-terminal 3V5 tag. Proteins were induced in *E. coli* with 0.1% arabinose at 30℃ for 1 h. **C**, Fluorescence images showing co-localization between Fha_sfGFP and TssB_mCherry2 in V52 Parental (*fha_sfGFP tssB_mCherry2*), Δ*tssM*, Δ*tssA*, and Δ*tssE*. A representative 30- × 30-μm field of cells with a 3× magnified 5- × 5-μm inset (marked by box) is shown. Scale bar: 5 μm. **D**, Quantification of cells forming Fha_sfGFP foci in Parental (*fha_sfGFP tssB_mCherry2*), fha^{L}, fha^{S}, and fha^{N} strains. Each data point represents the number of foci per cell quantified from an individual 30- × 30- μm field of view. **E**, Survival of killer strains during competition assays for which the survival of the prey is depicted in Figure 2G. **F**. Survival of killer strains during competition assays for which the survival of the prey is depicted in Figure 2I. For E and F, error bars indicate the mean +/- standard deviation of three biological replicates. **G**, Calibration of fluorescence intensity using $LacI^{mut}$_sfGFP-bound *lacO* arrays. The fluorescence intensities of sfGFP foci were quantified in *V. cholerae* V52 strains carrying *lacO3*,

lacO6, and *lacO13* arrays. Assuming that each *lacO* site binds two copies of LacI^{mut}_sfGFP, the number of bound fluorophores was used to generate a standard curve correlating sfGFP copy number with measured fluorescence intensity. **H**, Estimated sfGFP-equivalent copy numbers of Fha foci. Raw fluorescence intensities of Fha foci in *V. cholerae* V52 were converted into estimated sfGFP copy numbers using the calibration established in G.

Supplementary Figure 2. Functional characterization of Fha^{L} and Fha^{S}. A, DIC images of Fha^{N} at the indicated concentration. Scale bar: 5 μm. **B**, Bacterial two-hybrid analysis of Fha^{L}, Fha^{S}, and Fha^{N}. Proteins fused with the adenylate cyclase T25 or T18 subunits were co-expressed in the BTH101 reporter strain as indicated. A positive interaction is indicated by color development on X-Gal plates. **C**, Secretion analysis of Hcp in V52 wild-type, T6SS-null mutant Δ*tssM*, *fha*^{N}, and *fha*^{N} strains expressing plasmid-borne Fha and its variants, as indicated. **D**, Secretion analysis of Hcp in V52 wild-type, T6SS-null mutant Δ*tssM*, *fha*^{L}, and *fha*^{L} strains expressing plasmid-borne Fha and its variants, as indicated. For C and D, RpoB serves as a control for equal loading and autolysis.

Supplementary Figure 3. Identification of LLPS-disrupting mutations in Fha. A, Predicted structures of Fha^{S} using AlphaFold2. The predicted structures are colored based on the reported confidence of the AlphaFold modeling, from blue (pLDDT < 50) to red (pLDDT > 70). **B**, Fluorescence images showing the subcellular localization of plasmid-expressed Fha_sfGFP and its mutants in the V52 Δ*fha tssB_mCherry2* strain. Proteins were induced with 0.01% arabinose for 40 min prior to imaging. A representative 30- × 30-μm field of cells with a 3× magnified 5- × 5-μm inset (marked by box) is shown. Scale bar: 5 μm. **C**, Western blotting analysis of chromosomally encoded Fha in V52 *fha_sfGFP*, Δ*fha*, and *fha*^{L341A}*_sfGFP* strains. RpoB serves as a control for equal loading. **D**, Fluorescence images showing co-localization between TssL_sfGFP and TssB_mCherry2 in V52 Parental (*tssL_sfGFP tssB_mCherry2*) and *fha*^{L341A}. A representative 5- × 5-μm field of cells is shown. Scale bar: 1 μm. Quantification of cells forming TssL_sfGFP foci in Parental (*tssL_sfGFP tssB_mCherry2*) and *fha*^{L341A} is shown on the right. **E**, Fluorescence images showing co-localization between sfGFP_TssG and TssB_mCherry2 in V52 Parental (*sfGFP_tssG tssB_mCherry2*) and *fha*^{L341A}. A representative 5- × 5-μm field of cells is shown. Scale bar: 1 μm. Quantification of cells forming sfGFP_TssG foci in Parental (*sfGFP_tssG*

tssB_mCherry2) and *fha*^{L341A} is shown on the right. Each data point represents the number of foci per cell quantified from an individual 30- × 30- μm field of view. **F**, Survival of killer strains during competition assays for which the survival of the prey is depicted in Figure 3D. Error bars indicate the mean +/- standard deviation of three biological replicates. **G**, Time-lapse imaging of the V52 *fha_sfGFP* strain expressing plasmid-borne sfGFP, Fha_sfGFP, or Fha^{L341A}_sfGFP. Cells were imaged at 0 min and 60 min in the same field of view to monitor changes in pre-existing Fha_sfGFP foci. Proteins were induced for 1 h with 0.01% arabinose prior to imaging. A representative 30- × 30-μm field is shown. Scale bar: 5 μm.

Supplementary Figure 4. AlphaFold2-predicted structures of the Fha leucine-rich helix in complex with designed binders. The Fha leucine-rich helix is shown in magenta, and the binders are shown in light blue, with their N- and C-termini indicated. Residue L341 of Fha is highlighted with a blue box.

Supplementary Figure 5. Designed binders impair Fha foci formation and T6SS assembly. **A**, Fluorescence images showing the localization of chromosomally encoded Fha_sfGFP and TssB_mCherry2 in the V52 Parental (*fha_sfGFP tssB_mCherry2*) strains expressing designed binders. Binders were induced with 0.1% arabinose. **B**, Quantification of cells forming Fha_sfGFP foci in V52 Parental (*fha_sfGFP tssB_mCherry2*) strains expressing designed binders. **C**, Quantification of cells forming TssB_mCherry2 foci in V52 *fha_sfGFP tssB_mCherry2* strains expressing designed binders. Each data point represents the number of foci per cell quantified from an individual 30- × 30- μm field of view. Data points for the Parental carrying the empty vector and the *fha*^{L341A} mutant carrying the empty vector are reused from Fig. 3g (Fha_sfGFP foci) in B and from Fig. 3h (TssB_mCherry2 foci) in C. **D**, Fluorescence microscopy of plasmid-borne Fha_sfGFP in *E. coli* strains expressing designed binders. Fha_sfGFP and Binders were induced with 0.01% arabinose for 1 h before imaging. For A and D, a representative 30- × 30-μm field of cells with a 3× magnified 5- × 5-μm inset (marked by box) is shown. Scale bar: 5 μm. **E**, Western blotting analysis of plasmid-borne Fha_sfGFP expression in the *E. coli* strains shown in D. RpoB serves as a control for equal loading.

Supplementary Figure 6. Fha^{L} and Fha^{S} recruit distinct T6SS components. A, Volcano plot showing differentially enriched proteins identified by mass spectrometry in the pull-down assay. Lysates from V52 strains overexpressing the Strep-tagged Fha or sfGFP were used. Proteins enriched in the Fha pull-down (experimental group) compared to the sfGFP control (control group) were identified via mass spectrometry. The x-axis represents the $\log_2$ fold change in abundance of the identified proteins between the Fha and sfGFP samples, while the y-axis represents the $-\log_{10}$ adjusted *P*-value. Predicted T6SS-related proteins are highlighted in blue, and non-T6SS proteins are shown in gray. The Fha protein itself was excluded from this plot due to its exceptionally high abundance. All proteins identified by mass spectrometry are listed in Supplementary Data 4, and only proteins with 10 or more peptide hits were used to generate this volcano plot. **B**, Bacterial two-hybrid analysis of TssL cytoplasmic domain (TssL$_{cyto}$) interactions with Fha^{L}, Fha^{S}, and Fha^{N}. Proteins fused with the adenylate cyclase T25 or T18 subunits were co-expressed in the BTH101 reporter strain as indicated. A positive interaction is indicated by color development on X-Gal plates. **C**, Interaction of Fha and Fha^{L341A} with TssL and TssE. Pull-down analysis was conducted using His-tagged SUMO (control), SUMO-TssL, or SUMO-TssE, and FLAG-tagged MBP (control), Fha, or Fha^{L341A}. **D**, Fluorescence images showing recruitment of the TssL cytoplasmic domain (TssL$_{cyto}$) into Fha^{L} and Fha^{S} droplets. Fha^{L} and Fha^{S} proteins were mixed with MBP_sfGFP or sfGFP_TssL$_{cyto}$ at a ratio of 10: 1 in a 10% dextran-70 solution before imaging, respectively. A representative 30- × 30-μm field is shown. Scale bar: 5 μm. **E**, Quantification of GFP fluorescence intensity within Fha^{L} and Fha^{S} droplets. Statistical significance was calculated using Student's *t*-test, $*P < 0.05$.

Supplementary Figure 7. *fha^{L}* mutants display impaired intra-and inter- bacterial killing activities. A-D. Survival of killer strains during competition assays for which the survival of the prey is depicted in Figure 4 A-C, and 5 E. Error bars indicate the mean +/- standard deviation of at least three biological replicates and statistical significance was calculated using One-way ANOVA test for each group, $****P < 0.0001$.

Figure 1

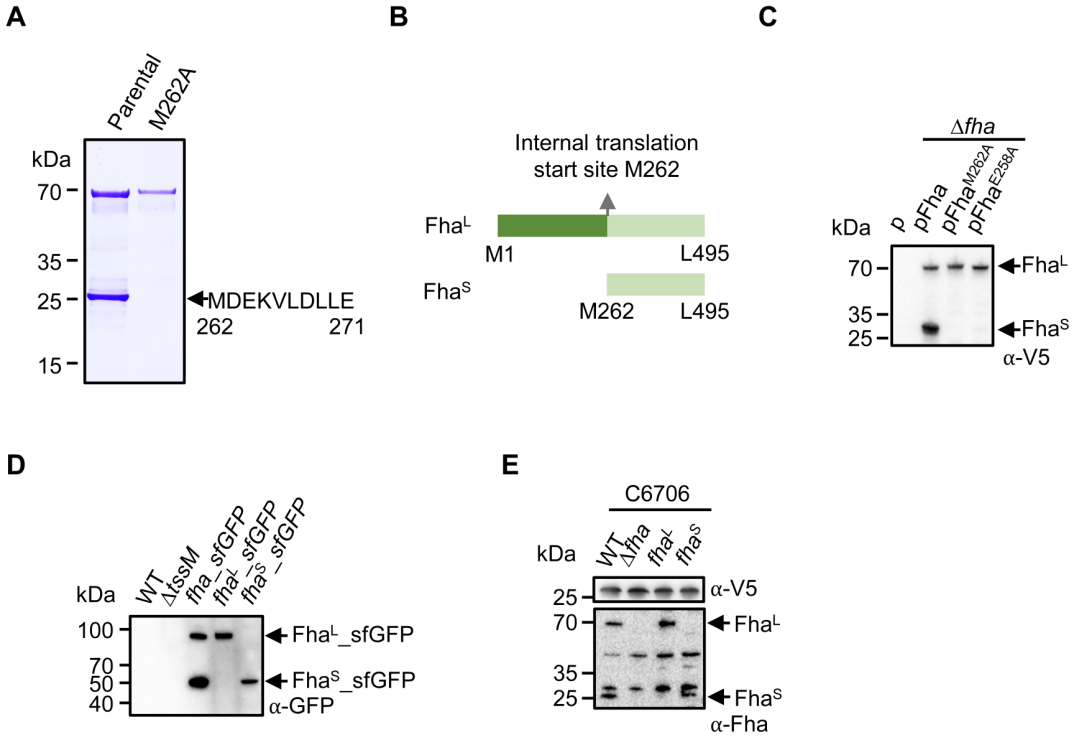

Figure 2

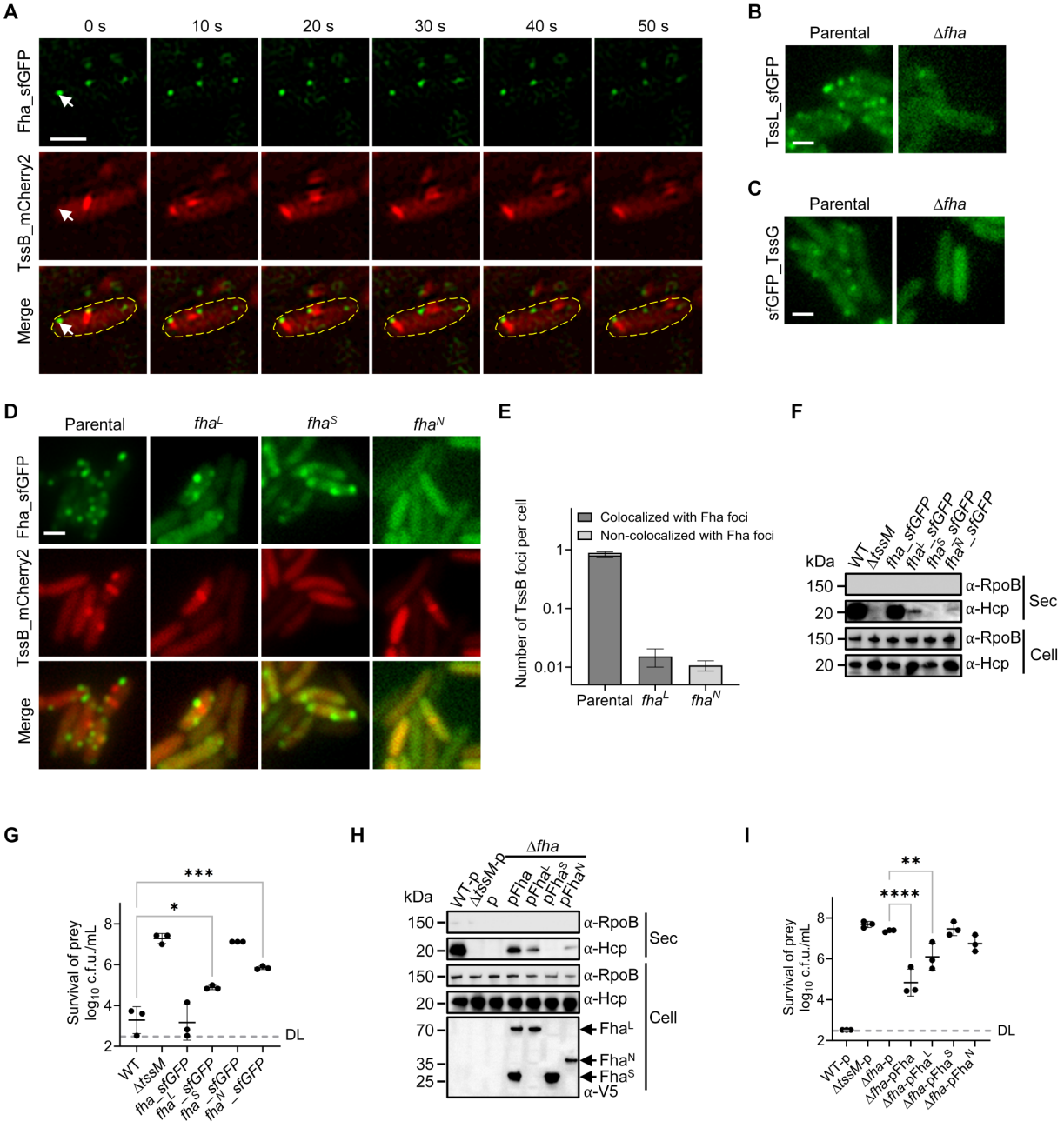

Figure 3

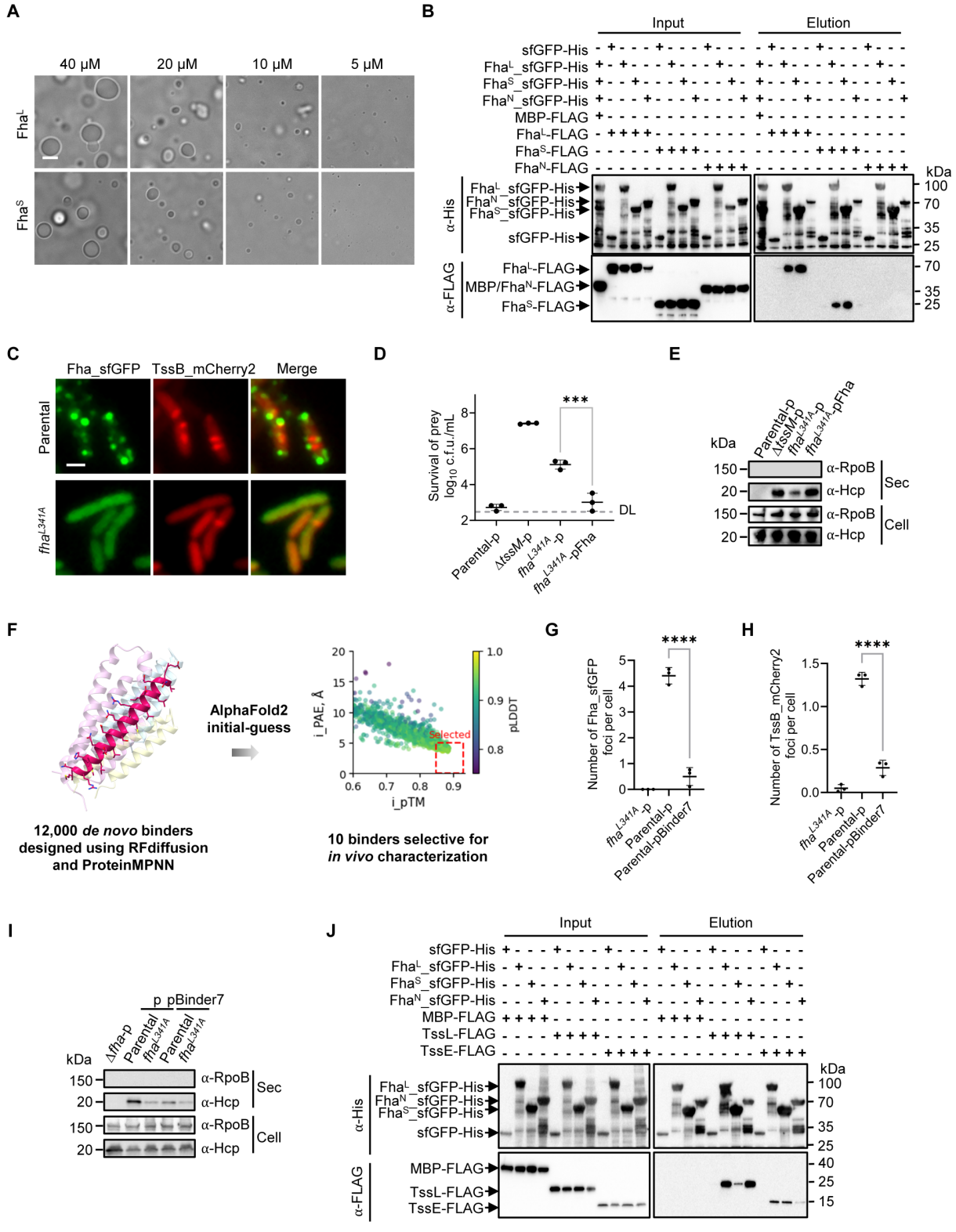

Figure 4

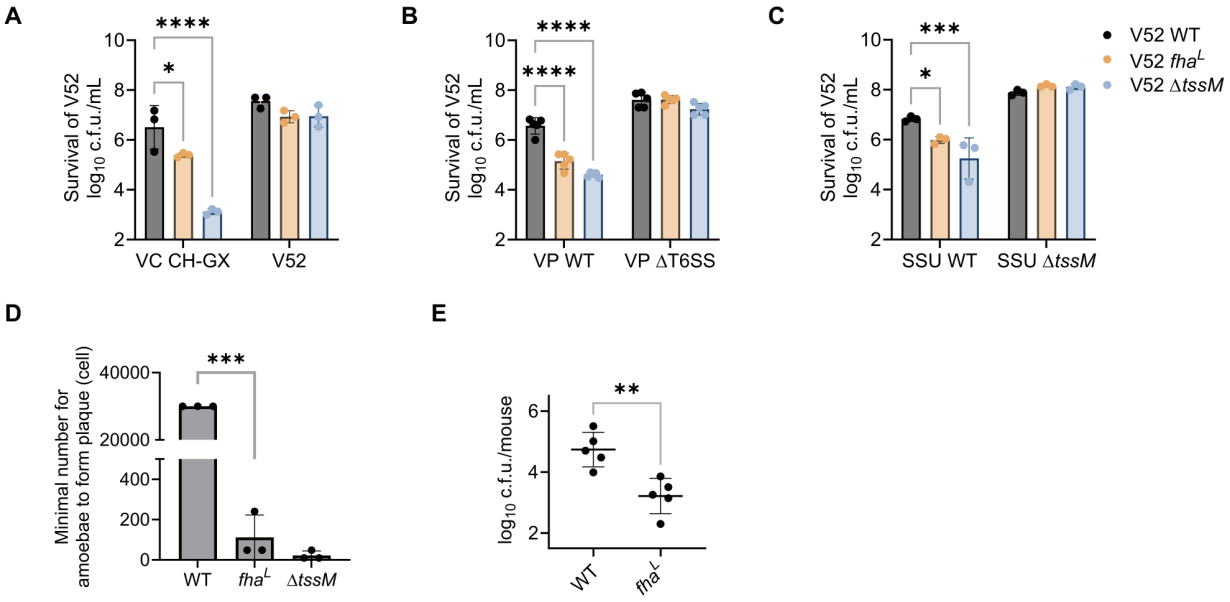

Figure 5

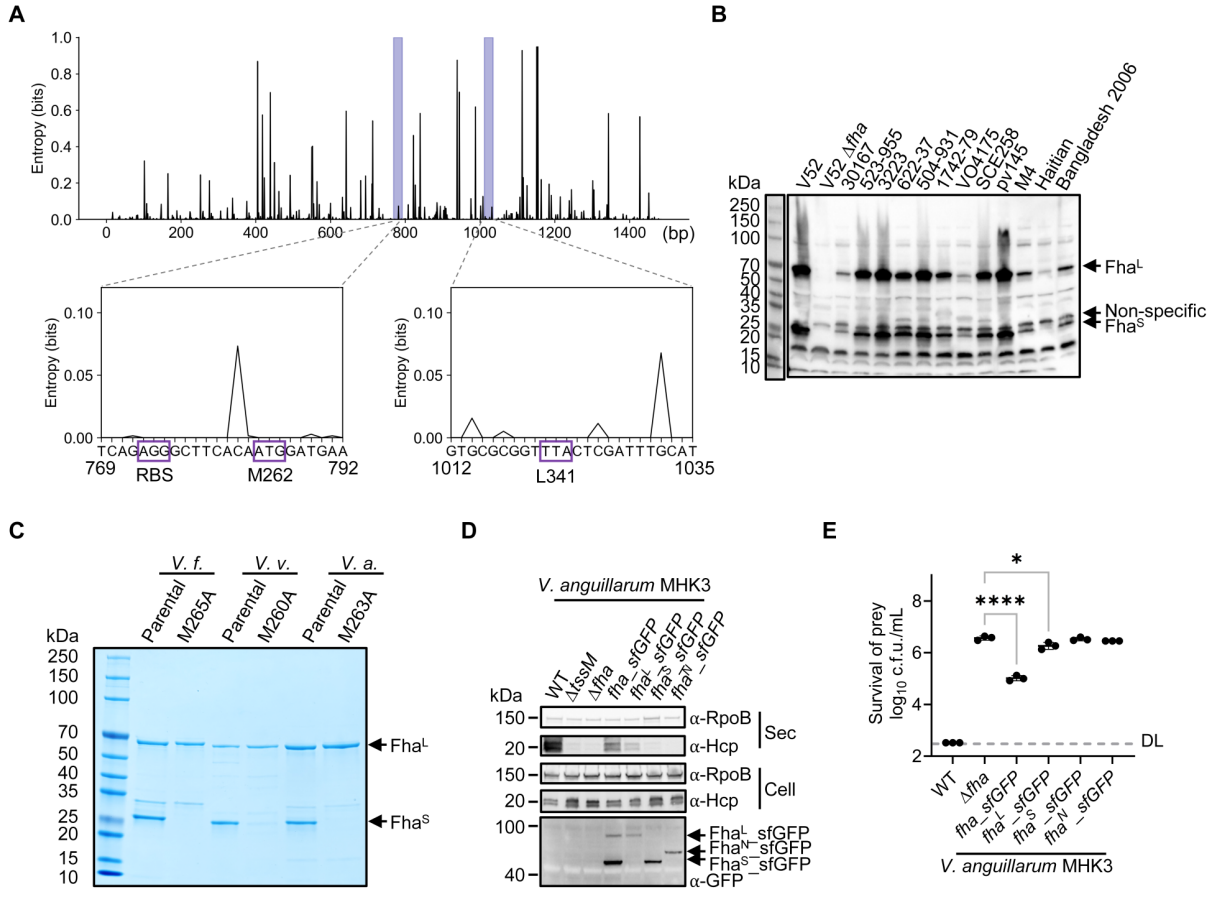

Figure 6